A Positivity-preserving High Order Finite Volume Compact-WENO Scheme for Compressible Euler Equations

Yan Guo · **Tao Xiong** · **Yufeng Shi**

Abstract In this paper, a positivity-preserving fifth-order finite volume compact-WENO scheme is proposed for solving compressible Euler equations. As we know, conservative compact finite volume schemes have high resolution properties while WENO (Weighted Essentially Non-Oscillatory) schemes are essentially non-oscillatory near flow discontinuities. We extend the idea of WENO schemes to some classical finite volume compact schemes [30], where lower order compact stencils are combined with WENO nonlinear weights to get a higher order finite volume compact-WENO scheme. The newly developed positivity-preserving limiter [44,42] is used to preserve positive density and internal energy for compressible Euler equations of fluid dynamics. The HLLC (Harten, Lax, and van Leer with Contact) approximate Riemann solver [37,4] is used to get the numerical flux at the cell interfaces. Numerical tests are presented to demonstrate the high-order accuracy, positivity-preserving, high-resolution and robustness of the proposed scheme.

1 Introduction

Computing numerical solutions of nonlinear hyperbolic systems of conservation laws is an interesting and challenging work. In recent years, a variety of high resolution schemes which are high order accurate for smooth solutions and non-oscillatory for discontinuous

Yan Guo
Department of Mathematics, China University of Mining and Technology, Xuzhou, Jiangsu 221116, P.R. China.
E-mail: yanguo@cumt.edu.cn

Tao Xiong
Department of Mathematics, University of Houston, Houston, Texas 77004, U.S.A.
E-mail: txiong@math.uh.edu

Yufeng Shi
School of Electric Power Engineering, China University of Mining and Technology, Xuzhou, Jiangsu 221116, P.R. China.
E-mail: shiyufeng@cumt.edu.cn

solutions without introducing spurious oscillations have been proposed for these problems. WENO schemes [25,19,33,34,3] have high order accuracy in smooth region and keep the essentially non-oscillatory properties for capturing shocks. However, these classical WENO schemes often suffer from poor spectral resolution and excessive numerical dissipation.

Compact schemes [22] have attracted a lot of attention due to its spectral-like resolution properties by using global grids. These schemes have the features of high-order accuracy with smaller stencils. However, linear compact schemes necessarily produce Gibbs-like oscillations when they are directly applied to flows with shock discontinuities, and the amplitude would not decrease with mesh refinement. To address this difficulty, several hybrid compact schemes are proposed to couple the ENO or WENO schemes for shock-turbulence interaction problems, e.g., a hybrid compact-ENO scheme by Adams and Shariff [1] and a hybrid compact-WENO scheme by Pirozzoli [30]. A new hybrid scheme as a weighted average of the compact scheme [30] and the WENO scheme [19] was developed by Ren et. al. [31]. Another compact scheme by treating the discontinuity as an internal boundary was proposed by Shen et. al. [32]. These hybrid schemes require indicators to detect discontinuities and switch to a non-compact scheme around discontinuities, spectral-like resolution properties would be lost.

A class of nonlinear compact schemes was proposed by Cockburn and Shu [8] for shock calculations. It was based on the cell-centered compact schemes [22] and combined with TVD or TVB limiters to control spurious numerical oscillations. Deng and Maekawa [9] and Deng and Zhang [10] developed a class of nonlinear compact schemes based on the ENO and WENO ideas respectively by adaptively choosing candidate stencils. Zhang et. al. [41] proposed increasingly higher order compact schemes based on higher order WENO reconstructions [3]. Instead of interpolating the conservative variables, they directly interpolated the flux by using the Lax-Friedrichs flux splitting and characteristic-wise projections. An improvement of the compact scheme converging to steady-state solutions of Euler equations was studies in [40]. A new linear central compact scheme was proposed in [26], both grid points and half grid points are evolved to get higher order accuracy and better resolutions.

Jiang et. al. [20] developed a class of weighted compact schemes based on the Padé type scheme of Lele [22]. It is a weighted combination of two biased third order compact stencils and a central fourth order compact stencil. A sixth order central compact scheme can be obtained in smooth regions. Recently Ghosh and Baeder employed the idea in [20], and developed a class of compact-reconstruction finite difference WENO schemes [13]. Lower order biased compact candidate stencils are identified at the cell interface and combined with the optimal nonlinear WENO weights. The resulting high order scheme is upwind. Their scheme was shown to be superior spectral accurate and non-oscillatory at discontinuities.

In this paper, we consider to design finite volume high order compact schemes for solving compressible Euler equations. A conservative formulation of the Euler equations is given by

$$U_t + F(U)_x = 0, \tag{1.1}$$

where U and $F(U)$ are vectors of conservative variables and fluxes respectively, which are given by

$$U = \begin{bmatrix} u_1 \\ u_2 \\ u_3 \end{bmatrix} = \begin{bmatrix} \rho \\ \rho u \\ E \end{bmatrix}, \quad F(U) = \begin{bmatrix} \rho u \\ \rho u^2 + p \\ u(E + p) \end{bmatrix},$$

with

$$E = \rho(\frac{1}{2}u^2 + e), \quad e = e(\rho, p) = \frac{p}{(\gamma - 1)\rho}, \tag{1.2}$$

where ρ is the density, p is the pressure, u is the particle velocity , E is the total energy per unit volume, e is the specific internal energy and γ is the ratio of specific heat ($\gamma = 1.4$ for ideal gas). The sound speed a is defined as

$$a = \sqrt{\frac{\gamma p}{\rho}}. \tag{1.3}$$

Physically, the density ρ and the pressure p should both be positive, and failure of preserving positive density or pressure may cause blow-up of the numerical solutions. Many first order schemes were shown to be positivity-preserving, such as Godunov-type schemes [11], flux vector splitting schemes [17], Lax-Friedrichs schemes [29,44], HLLC schemes [4] and gas-kinetic schemes [28,36]. Some second-order schemes were also developed based on these first order schemes, such as [11,36,29,12]. Recently Zhang and Shu have developed positivity-preserving methods for high order discontinuous Galerkin (DG) methods [44,45, 47], finite volume and finite difference WENO schemes [42,46]. Self-adjusting and positivity preserving high order schemes were developed by Balsara for MHD equations [2]. Hu et. al. have developed positivity-preserving high-order conservative schemes by using a flux cut-off method for solving compressible Euler equations [18]. Xiong et. al have developed a parametrized positivity preserving flux limiters for finite difference schemes solving compressible Euler equations [39].

In the present paper, we will develop a conservative positivity-preserving fifth-order finite volume compact-WENO (FVCW) scheme for compressible Euler equations. We employ the main idea in [13] where lower order compact stencils are combined with the optimal WENO weights to yield a fifth-order upwind compact interpolation. As an alternative to the finite difference compact interpolation in [13], we design a finite volume compact upwind scheme, which is more nature and can be easily used on unstructured meshes. We also employ the newly developed positivity-preserving rescaling limiter in [44,42] to preserve positive density and internal energy, which is very important in some extreme cases, such as vacuum or near vacuum solutions. The HLLC approximate Riemann solver [37,4] will be used as the numerical flux at the element interfaces due to its less dissipation and robustness for solving compressible Euler equations. The first order finite volume scheme with the HLLC flux is proved to preserve positive density and internal energy. We will show that the high order finite volume compact scheme with the positivity preserving rescaling limiter, can maintain high order accuracy similarly as the non-compact finite volume schemes. Numerical experiments will be presented to demonstrate the high spectral accuracy, high resolution, positivity-preserving and robustness of our proposed approach.

The rest of the paper is organized as follows. In Section 2, the positivity-preserving finite volume compact-WENO scheme for compressible Euler equations is presented. Numerical tests for some benchmark problems of compressible Euler equations are studied in Section 3. Conclusions are made in Section 4.

2 Positivity-preserving finite volume compact-WENO scheme

2.1 Finite volume scheme for compressible Euler equations

In this section, we first introduce the finite volume scheme [23] for compressible Euler equations (1.1) . The computational domain $[a,b]$ is divided into N cells as follows

$$a = x_{\frac{1}{2}} < x_{\frac{3}{2}} < \cdots < x_{N+\frac{1}{2}} = b.$$

The cells are denoted by $I_j = [x_{j-\frac{1}{2}}, x_{j+\frac{1}{2}}]$ with the cell center $x_j = \frac{1}{2}(x_{j-\frac{1}{2}} + x_{j+\frac{1}{2}})$ and the cell size $\Delta x_j = x_{j+\frac{1}{2}} - x_{j-\frac{1}{2}}$. If we integrate equation (1.1) over cell I_j, we obtain

$$\frac{\partial}{\partial t} \int_{x_{j-\frac{1}{2}}}^{x_{j+\frac{1}{2}}} U dx + F(U(x_{j+\frac{1}{2}}, t)) - F(U(x_{j-\frac{1}{2}}, t)) = 0. \tag{2.1}$$

The cell average of I_j is defined as

$$\bar{U}_j = \frac{1}{\Delta x_j} \int_{x_{j-\frac{1}{2}}}^{x_{j+\frac{1}{2}}} U(x, t) dx, \tag{2.2}$$

and the finite volume conservative scheme for (2.1) is

$$\frac{d\bar{U}_j(t)}{dt} = -\frac{1}{\Delta x_j}(\hat{F}_{j+\frac{1}{2}} - \hat{F}_{j-\frac{1}{2}}), \tag{2.3}$$

where the numerical flux $\hat{F}_{j+\frac{1}{2}}$ is a vector function of mass, momentum and total energy at the cell boundary and is defined by

$$\hat{F}_{j+\frac{1}{2}} = \hat{F}(U_{j+\frac{1}{2}}^-, U_{j+\frac{1}{2}}^+). \tag{2.4}$$

In this paper, $U_{j+\frac{1}{2}}^-$ and $U_{j+\frac{1}{2}}^+$ are obtained from a high order compact-WENO reconstruction, which will be discussed in the following subsections.

2.2 Compact-WENO reconstruction for scalars

For simplicity, we consider uniform grids with cell size $\Delta x_j = h = \frac{b-a}{N}, \forall j$ in this paper. We first review the finite volume compact reconstruction proposed in [30]. For a scalar variable $u(x)$, a compact representation around the grid node $x_{j+\frac{1}{2}}$ can be written as

$$\sum_{l=-L_1}^{L_2} \alpha_l \tilde{u}_{j+\frac{1}{2}+l} = \sum_{m=-M_1}^{M_2} a_m \bar{u}_{j+m}, \tag{2.5}$$

where $\tilde{u}_{j+\frac{1}{2}}$ denotes the reconstruction value of $u(x)$ at the grid node $x_{j+\frac{1}{2}}$. Assuming that the function u can be expanded by Taylor series up to K-th order around $x_{j+\frac{1}{2}}$

$$u(x) = \sum_{n=0}^{K-1} u_{j+\frac{1}{2}}^{(n)} \frac{(x - x_{j+\frac{1}{2}})^n}{n!} + O(h^K), \tag{2.6}$$

we have

$$\tilde{u}_{j+\frac{1}{2}+l} = \sum_{n=0}^{K-1} u_{j+\frac{1}{2}}^{(n)} \frac{l^n}{n!} h^n + O(h^K), \tag{2.7}$$

$$\bar{u}_{j+m} = \sum_{n=0}^{K-1} u_{j+\frac{1}{2}}^{(n)} \frac{1}{(n+1)!} [m^{n+1} - (m-1)^{n+1}] h^n + O(h^K). \tag{2.8}$$
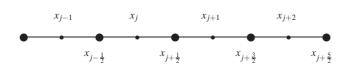
Fig. 2.1 Candidate stencils for interior points

A fifth-order compact upwind scheme in this class is for $K = 5$, which can yield the following scheme by taking $L_1 = L_2 = M_1 = M_2 = 1$ in (2.5),

$$\frac{3}{10}\tilde{u}_{j-\frac{1}{2}} + \frac{6}{10}\tilde{u}_{j+\frac{1}{2}} + \frac{1}{10}\tilde{u}_{j+\frac{3}{2}} = \frac{1}{30}\bar{u}_{j-1} + \frac{19}{30}\bar{u}_{j} + \frac{10}{30}\bar{u}_{j+1}. \tag{2.9}$$

Symmetrically, we also have

$$\frac{1}{10}\tilde{u}_{j-\frac{1}{2}} + \frac{6}{10}\tilde{u}_{j+\frac{1}{2}} + \frac{3}{10}\tilde{u}_{j+\frac{3}{2}} = \frac{10}{30}\bar{u}_{j} + \frac{19}{30}\bar{u}_{j+1} + \frac{1}{30}\bar{u}_{j+2}. \tag{2.10}$$

These classical fifth order linear finite volume compact schemes (2.9) and (2.10) based on smaller stencils are very accurate and keep good resolutions in smooth regions, but unacceptable non-physical oscillations are generated when they are directly applied to problems with discontinuities and the amplitude would not decrease as the grid nodes are refined.

In the following, we adopt the main idea of [13] to form a nonlinear finite volume compact-WENO scheme. For a fifth order finite volume compact-WENO scheme, three third-order compact stencils will be used as candidates, as shown in Fig.2.1. From (2.5), for the three candidate stencils, we have

$$\begin{aligned}
\frac{2}{3}u_{j-\frac{1}{2}}^{(0)} + \frac{1}{3}u_{j+\frac{1}{2}}^{(0)} &= \frac{1}{6}(\bar{u}_{j-1} + 5\bar{u}_{j}), \\
\frac{1}{3}u_{j-\frac{1}{2}}^{(1)} + \frac{2}{3}u_{j+\frac{1}{2}}^{(1)} &= \frac{1}{6}(5\bar{u}_{j} + \bar{u}_{j+1}), \\
\frac{2}{3}u_{j+\frac{1}{2}}^{(2)} + \frac{1}{3}u_{j+\frac{3}{2}}^{(2)} &= \frac{1}{6}(\bar{u}_{j} + 5\bar{u}_{j+1}).
\end{aligned} \tag{2.11}$$

Given the cell averages $\{\bar{u}_j\}$, a nonlinear weighted combination of (2.11) will result in

$$\begin{aligned}
&\frac{2\omega_0 + \omega_1}{3}\tilde{u}_{j-\frac{1}{2}} + \frac{\omega_0 + 2(\omega_1 + \omega_2)}{3}\tilde{u}_{j+\frac{1}{2}} + \frac{1}{3}\omega_2\tilde{u}_{j+\frac{3}{2}} \\
&= \frac{1}{6}\omega_0\bar{u}_{j-1} + \frac{5(\omega_0 + \omega_1) + \omega_2}{6}\bar{u}_{j} + \frac{\omega_1 + 5\omega_2}{6}\bar{u}_{j+1},
\end{aligned} \tag{2.12}$$

where the nonlinear weights $\{\omega_0, \omega_1, \omega_2\}$ will be specified later. Let $u_{j+\frac{1}{2}}^-$ denote the fifth order approximation of the nodal value $u(x_{j+\frac{1}{2}}, t^n)$ in cell I_j. From (2.12), a fifth order compact-WENO approximation of $u_{j+\frac{1}{2}}^-$ based on the stencil $\{x_{j-1}, x_j, x_{j+1}\}$ is given by

$$u_{j+\frac{1}{2}}^- = \tilde{u}_{j+\frac{1}{2}}. \tag{2.13}$$

In smooth regions, the finite volume compact-WENO scheme yields a fifth-order upwind compact scheme [30]. To construct a nonlinear compact scheme, we choose a set of normalized nonlinear weights ω_k [5,6] by taking

$$\omega_k = \frac{\alpha_k^z}{\sum_{l=0}^{2}\alpha_l^z}, \quad \alpha_k^z = c_k\left(1 + \left(\frac{\tau_5}{\beta_k + \varepsilon}\right)^2\right), \quad k = 0, 1, 2, \tag{2.14}$$

where $\tau_5 = |\beta_2 - \beta_0|$ and the classical smooth indicators β_k $(k = 0, 1, 2)$ [33] are given by

$$\beta_0 = \frac{13}{12}(\bar{u}_{j-2} - 2\bar{u}_{j-1} + \bar{u}_j)^2 + \frac{1}{4}(\bar{u}_{j-2} - 4\bar{u}_{j-1} + 3\bar{u}_j)^2,$$

$$\beta_1 = \frac{13}{12}(\bar{u}_{j-1} - 2\bar{u}_j + \bar{u}_{j+1})^2 + \frac{1}{4}(\bar{u}_{j-1} - \bar{u}_{j+1})^2,$$

$$\beta_2 = \frac{13}{12}(\bar{u}_j - 2\bar{u}_{j+1} + \bar{u}_{j+2})^2 + \frac{1}{4}(3\bar{u}_j - 4\bar{u}_{j+1} + \bar{u}_{j+2})^2.$$

ε is a small positive number to avoid the denominator to be 0, in our numerical tests, we take $\varepsilon = 10^{-13}$. The optimal linear weights are $c_0 = \frac{2}{10}, c_1 = \frac{5}{10}, c_2 = \frac{3}{10}$. The weights (2.14) are denoted as WENO-Z weights, which can avoid accuracy lost at critical points [5].

For the scalar case, a tri-diagonal system (2.12) is solved to get $u^-_{j+\frac{1}{2}}$. Let $u^+_{j+\frac{1}{2}}$ denote the fifth order approximation of the nodal value $u(x_{j+\frac{1}{2}}, t^n)$ from cell I_{j+1}, following a similar procedure as above, it can be obtained by the stencil $\{x_j, x_{j+1}, x_{j+2}\}$. Similar to classical WENO schemes, near critical points, the corresponding weight approaches to 0 and the system reduces to a biased bidiagonal system. Across the discontinuities, the fifth-order scheme yields a third-order compact scheme which has higher resolution than a third order non-compact scheme.

2.3 Compact-WENO reconstruction for systems

In this subsection, we will describe the finite volume compact-WENO reconstruction for compressible Euler equations. The scalar algorithm (2.12) in the previous subsection will be applied along each characteristic field. As we know, the conservative Euler equations (1.1) can also be written in a quasi-linear form [37]

$$U_t + A(U)U_x = 0, \tag{2.15}$$

where the coefficient matrix $A(U)$ is the Jacobian matrix of $F(U)$ and can be written as

$$A(U) = \begin{bmatrix} 0 & 1 & 0 \\ -\frac{1}{2}(\gamma-3)(\frac{u_2}{u_1})^2 & (3-\gamma)(\frac{u_2}{u_1}) & \gamma-1 \\ -\frac{\gamma u_2 u_3}{u_1^2} + (\gamma-1)(\frac{u_2}{u_1})^3 & \frac{\gamma u_3}{u_1} - \frac{3}{2}(\gamma-1)(\frac{u_2}{u_1})^2 & \gamma(\frac{u_2}{u_1}) \end{bmatrix}.$$

The total specific enthalpy H is related to the specific enthalpy h, they are

$$H = \frac{E+p}{\rho} \equiv \frac{1}{2}u^2 + h, \quad h = e + \frac{p}{\rho}. \tag{2.16}$$

The eigenvalues of the Jacobian matrix $A(U)$ are

$$\lambda_1 = u - a, \quad \lambda_2 = u, \quad \lambda_3 = u + a, \tag{2.17}$$

where a is the speed of sound (1.3). The corresponding right eigenvectors are

$$r^{(1)} = \begin{bmatrix} 1 \\ u-a \\ H-ua \end{bmatrix}, \quad r^{(2)} = \begin{bmatrix} 1 \\ u \\ \frac{1}{2}u^2 \end{bmatrix}, \quad r^{(3)} = \begin{bmatrix} 1 \\ u+a \\ H+ua \end{bmatrix}.$$

A matrix $R(U)$ is formed by the right eigenvectors

$$R(U) = (r^{(1)}, r^{(2)}, r^{(3)}). \tag{2.18}$$

Letting $L(U) = R(U)^{-1}$, then

$$L(U)A(U)R(U) = \Lambda,$$

here Λ is the diagonal matrix $\Lambda = diag(\lambda_1, \lambda_2, \lambda_3)$. Denoting a vector $l^{(k)}$ to be the k-th row in $L(U)$, then

$$
\begin{aligned}
l^{(1)} &= \frac{1}{2}(c_2 + u/a, -c_1 u - 1/a, c_1), \\
l^{(2)} &= (1 - c_2, c_1 u, -c_1), \\
l^{(3)} &= \frac{1}{2}(c_2 - u/a, -c_1 u + 1/a, c_1),
\end{aligned}
\tag{2.19}
$$

where $c_1 = (\gamma - 1)/a^2$, $c_2 = \frac{1}{2}u^2 c_1$.

At the grid node $x_{j+\frac{1}{2}}$, denoting $U^-_{j+\frac{1}{2}}$ as the fifth order approximation of the nodal values $U(x_{j+\frac{1}{2}}, t^n)$ at time t^n within the cells I_j, the scalar finite volume compact-WENO reconstruction (2.12) is applied to each component of the characteristic variables $\bar{V}_j = L(U^{Roe}_{j+\frac{1}{2}})\bar{U}_j$ to obtain $U^-_{j+\frac{1}{2}}$, where $U^{Roe}_{j+\frac{1}{2}}$ denotes the Roe-average of the cell-average values $\bar{U}_j$ and $\bar{U}_{j+1}$ [37].

For the systems, a characteristic-wise finite volume compact-WENO scheme consists of the following steps:

1. At each grid node $x_{j+\frac{1}{2}}$, computing the eigenvalues (2.17) and eigenvectors (2.18) and (2.19) by using $U^{Roe}_{j+\frac{1}{2}}$.
2. Along each characteristic field, computing the weights (2.14) from characteristic variables $\bar{V}_j = L(U^{Roe}_{j+\frac{1}{2}})\bar{U}_j$.
3. Applying the scalar reconstruction (2.12) at each characteristic field

$$
\begin{aligned}
&a^{(k)}_{j+\frac{1}{2}} l^{(k)}_{j+\frac{1}{2}} \tilde{U}_{j-\frac{1}{2}} + b^{(k)}_{j+\frac{1}{2}} l^{(k)}_{j+\frac{1}{2}} \tilde{U}_{j+\frac{1}{2}} + c^{(k)}_{j+\frac{1}{2}} l^{(k)}_{j+\frac{1}{2}} \tilde{U}_{j+\frac{3}{2}} \\
&= d^{(k)}_{j+\frac{1}{2}} l^{(k)}_{j+\frac{1}{2}} \bar{U}_{j-1} + e^{(k)}_{j+\frac{1}{2}} l^{(k)}_{j+\frac{1}{2}} \bar{U}_j + f^{(k)}_{j+\frac{1}{2}} l^{(k)}_{j+\frac{1}{2}} \bar{U}_{j+1}
\end{aligned}
\tag{2.20}
$$

for $k = 1, 2, 3$. The coefficients $a^{(k)}_{j+\frac{1}{2}}, b^{(k)}_{j+\frac{1}{2}}, c^{(k)}_{j+\frac{1}{2}}, d^{(k)}_{j+\frac{1}{2}}, e^{(k)}_{j+\frac{1}{2}}, f^{(k)}_{j+\frac{1}{2}}$ corresponding to the coeffcients in (2.12), which can be obtained from Step 2.

4. Rewriting the equation (2.20) to be

$$A_{j+\frac{1}{2}}\tilde{U}_{j-\frac{1}{2}} + B_{j+\frac{1}{2}}\tilde{U}_{j+\frac{1}{2}} + C_{j+\frac{1}{2}}\tilde{U}_{j+\frac{3}{2}} = D_{j+\frac{1}{2}}\bar{U}_{j-1} + E_{j+\frac{1}{2}}\bar{U}_j + F_{j+\frac{1}{2}}\bar{U}_{j+1} \tag{2.21}$$

where

$$
A_{j+\frac{1}{2}} = \begin{bmatrix} a^{(1)}_{j+\frac{1}{2}} l^{(1)}_{j+\frac{1}{2}} \\ a^{(2)}_{j+\frac{1}{2}} l^{(2)}_{j+\frac{1}{2}} \\ a^{(3)}_{j+\frac{1}{2}} l^{(3)}_{j+\frac{1}{2}} \end{bmatrix}, B_{j+\frac{1}{2}} = \begin{bmatrix} b^{(1)}_{j+\frac{1}{2}} l^{(1)}_{j+\frac{1}{2}} \\ b^{(2)}_{j+\frac{1}{2}} l^{(2)}_{j+\frac{1}{2}} \\ b^{(3)}_{j+\frac{1}{2}} l^{(3)}_{j+\frac{1}{2}} \end{bmatrix}, C_{j+\frac{1}{2}} = \begin{bmatrix} c^{(1)}_{j+\frac{1}{2}} l^{(1)}_{j+\frac{1}{2}} \\ c^{(2)}_{j+\frac{1}{2}} l^{(2)}_{j+\frac{1}{2}} \\ c^{(3)}_{j+\frac{1}{2}} l^{(3)}_{j+\frac{1}{2}} \end{bmatrix},
$$

$$D_{j+\frac{1}{2}} = \begin{bmatrix} d^{(1)}_{j+\frac{1}{2}} l^{(1)}_{j+\frac{1}{2}} \\ d^{(2)}_{j+\frac{1}{2}} l^{(2)}_{j+\frac{1}{2}} \\ d^{(3)}_{j+\frac{1}{2}} l^{(3)}_{j+\frac{1}{2}} \end{bmatrix}, E_{j+\frac{1}{2}} = \begin{bmatrix} e^{(1)}_{j+\frac{1}{2}} l^{(1)}_{j+\frac{1}{2}} \\ e^{(2)}_{j+\frac{1}{2}} l^{(2)}_{j+\frac{1}{2}} \\ e^{(3)}_{j+\frac{1}{2}} l^{(3)}_{j+\frac{1}{2}} \end{bmatrix}, F_{j+\frac{1}{2}} = \begin{bmatrix} f^{(1)}_{j+\frac{1}{2}} l^{(1)}_{j+\frac{1}{2}} \\ f^{(2)}_{j+\frac{1}{2}} l^{(2)}_{j+\frac{1}{2}} \\ f^{(3)}_{j+\frac{1}{2}} l^{(3)}_{j+\frac{1}{2}} \end{bmatrix}.$$

Noticing that $l^{(k)}_{j+\frac{1}{2}}$ for $k = 1, 2, 3$ are all vectors, a 3×3 block tri-diagonal system (2.21) is solved by using the chasing method [15] to obtain $\tilde{U}_{j+\frac{1}{2}}$.

From (2.21), a fifth order compact-WENO approximation of $U^-_{j+\frac{1}{2}}$ based on the stencil $\{x_{j-1}, x_j, x_{j+1}\}$ is given by

$$U^-_{j+\frac{1}{2}} = \tilde{U}_{j+\frac{1}{2}}. \tag{2.22}$$

Letting $U^+_{j+\frac{1}{2}}$ denote the fifth order approximation of the nodal value $U(x_{j+\frac{1}{2}}, t^n)$ from cell I_{j+1}, following a similar procedure as above, it can be obtained by the stencil $\{x_j, x_{j+1}, x_{j+2}\}$.

2.4 Positivity-preserving and HLLC approximate Riemann solver

For compressible Euler equations, the Riemann solutions consist of a contact wave and two acoustic waves, either may be a shock or a rarefaction wave. In [14], Godunov presented a first-order upwind scheme which could capture shock waves without introducing nonphysical spurious oscillations. The important part of the Godunov-type method is the exact or approximate solutions of the Riemann problem. Exact solutions to the Riemann problem is difficult or too expensive to be obtained. Approximate Riemann solvers are often used to build Godunov-type numerical schemes. The HLLC approximate Riemann solver [37, 4] has been proved to be very simple, reliable and robust. In [4], Batten et al. proposed an appropriate choice of the acoustic wavespeeds required by HLLC and proved that the resulting numerical method resolves isolated shock and contact waves exactly, and is positively conservative which will be reviewed in the following.

For the HLLC flux, two averaged states U^*_l, U^*_r between the two acoustic waves S_L, S_R are considered, which are separated by the contact wave whose speed is denoted by S_M. The approximate Riemann solution with two states U_l and U_r is defined as

$$U^{HLLC} = \begin{cases} U_l, & \text{if } S_L > 0, \\ U^*_l, & \text{if } S_L \leq 0 < S_M, \\ U^*_r, & \text{if } S_M \leq 0 \leq S_R, \\ U_r, & \text{if } S_R < 0. \end{cases} \tag{2.23}$$

The corresponding flux is

$$\hat{F}^{HLLC}(U_l, U_r) = \begin{cases} F_l, & \text{if } S_L > 0, \\ F^*_l = F_l + S_L(U^*_l - U_l), & \text{if } S_L \leq 0 < S_M, \\ F^*_r = F_r + S_r(U^*_r - U_r), & \text{if } S_M \leq 0 \leq S_R, \\ F_r, & \text{if } S_R < 0. \end{cases} \tag{2.24}$$

where $F_l = F(U_l)$ and $F_r = F(U_r)$, similarly for the following variables with subscripts l and r.

To determine U^*_l, the following assumption has been made [4]

$$S_M = u^*_l = u^*_r = u^*. \tag{2.25}$$

which gives the contact wave velocity

$$S_M = \frac{\rho_r u_r (S_R - u_r) - \rho_l u_l (S_L - u_l) + p_l - p_r}{\rho_l (S_R - u_r) - \rho_l (S_L - u_l)}.$$ (2.26)

and

$$\begin{cases} \rho_l^* = \rho_l \frac{S_L - u_l}{S_L - S_M}, \\ p^* = \rho_l (u_l - S_L)(u_l - S_M) + p_l, \\ \rho_l^* u_l^* = \frac{(S_L - u_l)\rho_l u_l + (p^* - p_l)}{S_L - S_M}, \\ E_l^* = \frac{(S_L - u_l) E_l - p_l u_l + p^* S_M}{S_L - S_M}. \end{cases}$$ (2.27)

The right star state can be obtained symmetrically.

To make the scheme preserving positivity, the acoustic wavespeeds are computed from

$$S_L = \min[u_l - a_l, \tilde{u}^* - \tilde{a}^*], \quad S_R = \min[u_r + a_r, \tilde{u}^* + \tilde{a}^*],$$ (2.28)

where

$$\begin{cases} \tilde{u}^* = \frac{u_l + u_r R_\rho}{1 + R_\rho}, \\ \tilde{a}^* = \sqrt{(\gamma - 1)[\tilde{H}^* - \frac{1}{2}\tilde{u}^{*2}]}, \\ \tilde{H}^* = \frac{(H_l + H_r R_\rho)}{1 + R_\rho}, \\ R_\rho = \sqrt{\frac{\rho_r}{\rho_l}}. \end{cases}$$ (2.29)

Defining the set of physically realistic states as those with positive densities and internal energies by

$$G = \left\{ U = \begin{bmatrix} \rho \\ \rho u \\ E \end{bmatrix}, \rho > 0, e = \frac{E}{\rho} - \frac{u^2}{2} > 0 \right\},$$ (2.30)

then G is a convex set [4].

We now consider a first order finite volume scheme

$$\bar{U}_j^{n+1} = \bar{U}_j^n - \lambda[\hat{F}(\bar{U}_j^n, \bar{U}_{j+1}^n) - \hat{F}(\bar{U}_{j-1}^n, \bar{U}_j^n)],$$ (2.31)

where $\hat{F}(\cdot, \cdot)$ is a HLLC flux and $\lambda = \frac{\Delta t}{h}$. For a positively conservative scheme (2.31), if $\bar{U}_j^n, j = 1, \cdots, N$, is contained in G, then $\bar{U}_j^{n+1}, j = 1, \cdots, N$, will also lie inside G. This would be guaranteed by proving the intermediate states $U_l^* \in G$ if we have $U_l \in G$, and proving $U_r^* \in G$ if we have $U_r \in G$, because G is a convex set (for details see [4]).

In the following, we will show the left star state $U_l^* \in G$, while similar arguments hold for the right star state $U_r^* \in G$. That is, when $U_l \in G$, which is equivalent to

$$\rho_l > 0, \quad E_l - \frac{1}{2}\rho_l u_l^2 > 0,$$ (2.32)

we will have

$$\rho_l^* > 0,$$ (2.33)

and

$$E_l^* - \frac{1}{2}\rho_l^* u_l^{*2} > 0.$$ (2.34)

From (2.27), we can get

$$\rho_l^* = \rho_l \frac{S_L - u_l}{S_L - S_M}.$$ (2.35)

S_M in (2.26) is an averaged velocity, from (2.28) we have

$$S_L < S_M, \quad S_L < u_l, \tag{2.36}$$

and $\rho_l^* > 0$ is easily obtained. Using relations (2.27) and (2.36), (2.34) can be rewritten as

$$(u_l - S_L)E_l + p_l u_l - p^* S_M + \frac{((S_L - u_l)\rho_l u_l - p_l + p^*)^2}{2\rho_l(S_L - u_l)} > 0, \tag{2.37}$$

which is equivalent to

$$\frac{1}{2}\rho_l(S_M - u_l)^2 - p_l\frac{S_M - u_l}{u_l - S_L} + \frac{p_l}{\gamma - 1} > 0. \tag{2.38}$$

To guarantee this inequality for any value of $S_M - u_l$, the discriminant of the above quadratic function of $S_M - u_l$ should be negative, which gives the following condition

$$\frac{p_l^2}{(u_l - S_L)^2} - 2\rho_l^2 e_l < 0, \tag{2.39}$$

that is

$$S_L < u_l - \frac{p_l}{\rho_l\sqrt{2e_l}} = u_l - \sqrt{\frac{\gamma - 1}{2\gamma}}\sqrt{\frac{\gamma p_l}{\rho_l}} = u_l - \sqrt{\frac{\gamma - 1}{2\gamma}}a_l, \tag{2.40}$$

which is always satisfied with acoustic wavespeeds (2.28).

Remark 1 As in [44], if we consider the first order finite volume scheme (2.31) with the HLLC flux (2.24) and averaged intermediate states (2.27) for solving the compressible Euler equations (1.1), this first order scheme is positivity-preserving with the choice of the acoustic wavespeeds (2.28) and under the following CFL condition

$$\lambda \||u| + a\|_\infty \le 1. \tag{2.41}$$

Now to design a positivity-preserving fifth-order finite volume compact-WENO scheme, we first consider the Euler forward time discretization for equation (2.3)

$$\bar{U}_j^{n+1} = \bar{U}_j^n - \lambda(\hat{F}(U_{j+\frac{1}{2}}^-, U_{j+\frac{1}{2}}^+) - \hat{F}(U_{j-\frac{1}{2}}^-, U_{j-\frac{1}{2}}^+), \tag{2.42}$$

where $\hat{F}$ is the HLLC flux, $U_{j+\frac{1}{2}}^-$ and $U_{j+\frac{1}{2}}^+$ are obtained by using the compact-WENO reconstructions in Section 2.3. We employ the idea in [42,44] to construct high order finite volume compact-WENO schemes to preserve positive density and pressure or internal energy for the Euler system.

We consider a polynomial vector $Q_j(x) = (\rho_j(x)), (\rho u)_j(x), E_j(x))^T$ with degree $K(K \ge 2)$ on I_j, such that

$$U_{j-\frac{1}{2}}^+ = Q_j(x_{j-\frac{1}{2}}), \quad U_{j+\frac{1}{2}}^- = Q_j(x_{j+\frac{1}{2}}), \quad \bar{U}_{j+q} = \frac{1}{\Delta x}\int_{x_{j+q-\frac{1}{2}}}^{x_{j+q+\frac{1}{2}}} Q_j(x)dx, \tag{2.43}$$

here q is related to K, for example, if $K = 5$, $q = -1, 0, 1$. By using the M-point Gauss-Lobatto quadrature rule on I_j and choose the quadrature points as $S_j = \{x_{j-\frac{1}{2}} = \hat{x}_j^1, \cdots, \hat{x}_j^M = x_{j+\frac{1}{2}}\}$, a sufficient condition for $\bar{U}_j^{n+1} \in G$ is $Q_j(\hat{x}_j^\alpha) \in G$ for $\alpha = 1, 2, \cdots, M$, under a suitable CFL condition. We denote $\hat{\omega}_\alpha$ as the Legendre Gauss-Lobatto quadrature weights on the interval $[-\frac{1}{2}, \frac{1}{2}]$, and $\sum_{\alpha=1}^M \hat{\omega}_\alpha = 1$ with $2M - 3 \le K$. Following [44], we have

Theorem 1 *Consider the high order ($K \geq 2$) finite volume compact-WENO scheme (2.42) with the HLLC flux (2.24) for solving the compressible Euler equations (1.1). The first order scheme (2.31) with the HLLC flux would be positivity-preserving under the condition (2.28) with the averaged intermediate states (2.27). If the reconstructed polynomial vector $Q_j(x) = (\rho_j(x)), (\rho u)_j(x), E_j(x)$ (2.43) satisfies $Q_j(\hat{x}_j^\alpha) \in G, \forall j$, the scheme (2.42) is positivity-preserving ($\bar{U}_j^{n+1} \in G$) under the the CFL condition*

$$\lambda \, \||u| + a\|_\infty \leq \omega_1. \tag{2.44}$$

Proof The proof is similar to that in [44]. By using the M-point Gauss-Lobatto rule, the cell average $\bar{U}_j$ can be written as

$$\bar{U}_j = \frac{1}{\Delta x} \int_{x_{j-\frac{1}{2}}}^{x_{j+\frac{1}{2}}} Q_j(x)dx = \sum_{\alpha=1}^{M} \hat{\omega}_\alpha Q_j(\hat{x}_j^\alpha). \tag{2.45}$$

Noticing that $U_{j-\frac{1}{2}}^+ = Q_j(\hat{x}_j^1)$ and $U_{j+\frac{1}{2}}^- = Q_j(\hat{x}_j^M), \forall j$, the scheme (2.42) can be rearranged as follows

$$
\begin{aligned}
\bar{U}_j^{n+1} &= \sum_{\alpha=1}^{M} \hat{\omega}_\alpha Q_j(\hat{x}_j^\alpha) - \lambda \big(\hat{F}(U_{j+\frac{1}{2}}^-, U_{j+\frac{1}{2}}^+) - \hat{F}(U_{j-\frac{1}{2}}^+, U_{j+\frac{1}{2}}^-) + \hat{F}(U_{j-\frac{1}{2}}^+, U_{j+\frac{1}{2}}^-) - \hat{F}(U_{j-\frac{1}{2}}^-, U_{j-\frac{1}{2}}^+)\big) \\
&= \sum_{\alpha=2}^{M-1} \hat{\omega}_\alpha Q_j(\hat{x}_j^\alpha) + \hat{\omega}_1 \left(U_{j-\frac{1}{2}}^+ - \frac{\lambda}{\hat{\omega}_1} [\hat{F}(U_{j-\frac{1}{2}}^+, U_{j+\frac{1}{2}}^-) - \hat{F}(U_{j-\frac{1}{2}}^-, U_{j-\frac{1}{2}}^+)] \right) \\
&\quad + \hat{\omega}_M \left(U_{j+\frac{1}{2}}^- - \frac{\lambda}{\hat{\omega}_M} [\hat{F}(U_{j+\frac{1}{2}}^-, U_{j+\frac{1}{2}}^+) - \hat{F}(U_{j-\frac{1}{2}}^+, U_{j+\frac{1}{2}}^-)] \right) \\
&= \sum_{\alpha=2}^{M-1} \hat{\omega}_\alpha Q_j(\hat{x}_j^\alpha) + \hat{\omega}_1 H_1 + \hat{\omega}_M H_M,
\end{aligned}
$$

where

$$H_1 = U_{j-\frac{1}{2}}^+ - \frac{\lambda}{\hat{\omega}_1}[\hat{F}(U_{j-\frac{1}{2}}^+, U_{j+\frac{1}{2}}^-) - \hat{F}(U_{j-\frac{1}{2}}^-, U_{j-\frac{1}{2}}^+)],$$

$$H_M = U_{j+\frac{1}{2}}^- - \frac{\lambda}{\hat{\omega}_M}[\hat{F}(U_{j+\frac{1}{2}}^-, U_{j+\frac{1}{2}}^+) - \hat{F}(U_{j-\frac{1}{2}}^+, U_{j+\frac{1}{2}}^-)].$$

The above two equations are both of the form (2.31), therefore H_1 and H_M are in the set G due to $U_{j+\frac{1}{2}}^\pm \in G, \forall j$ and the CFL condition (2.44) with the HLLC flux (2.24) and the acoustic wavespeeds (2.28). Now $\bar{U}_j^{n+1} \in G$ is proved since it is a convex combination of H_1, H_M and $Q_j(\hat{x}_j^\alpha)$ for $2 \leq \alpha \leq M - 1$, which are all in G.

Similar to the approach in [42,44], the positivity-preserving limiter for the present scheme in the one-dimensional space will be constructed. The easy-implementation algorithm of WENO schemes in [42] will be adopted:

1. Set up a small positive parameter $\varepsilon = \min_j\{10^{-13}, \bar{\rho}_j^n\}$.
2. Compute the limiter

$$\theta_1 = \min \left\{ \frac{\bar{\rho}_j^n - \varepsilon}{\bar{\rho}_j^n - \rho_{min}}, 1 \right\}, \tag{2.46}$$

where $\rho_{min} = \{\rho_{j+\frac{1}{2}}^-, \rho_{j-\frac{1}{2}}^+, \rho_j(x_j^{1*})\}$ and

$$\rho_j(x_j^{1*}) = \frac{\bar{\rho}_j^n - \hat{\omega}_1 \rho_{j-\frac{1}{2}}^+ - \hat{\omega}_M \rho_{j+\frac{1}{2}}^-}{1 - 2\hat{\omega}_1}. \tag{2.47}$$

3. Modify the density by letting

$$\hat{\rho}_j(x) = \theta_1(\rho_j(x) - \bar{\rho}_j^n) + \bar{\rho}_j^n. \tag{2.48}$$

Get $\hat{\rho}_{j+\frac{1}{2}}^-$ and $\hat{\rho}_{j-\frac{1}{2}}^+$ from

$$\hat{\rho}_{j+\frac{1}{2}}^- = \theta_1(\rho_{j+\frac{1}{2}}^- - \bar{\rho}_j^n) + \bar{\rho}_j^n,$$
$$\hat{\rho}_{j-\frac{1}{2}}^+ = \theta_1(\rho_{j-\frac{1}{2}}^+ - \bar{\rho}_j^n) + \bar{\rho}_j^n.$$

Denote

$$\hat{W}_j^1 = \hat{U}_{j+\frac{1}{2}}^-, \quad \hat{W}_j^2 = \hat{U}_{j-\frac{1}{2}}^+, \quad \hat{W}_j^3 = \frac{\bar{U}_j^n - \hat{\omega}_1 \hat{U}_{j-\frac{1}{2}}^+ - \hat{\omega}_M \hat{U}_{j+\frac{1}{2}}^-}{1 - 2\hat{\omega}_1}.$$

4. Get $\theta_2 = \min_{\alpha=1,2,3} t_\varepsilon^\alpha$ from modifying the internal energy:
   For $\alpha = 1,2,3$:
   – if $e(\hat{W}_j^\alpha) < \varepsilon$, solve the following quadratic equations for t_ε^α as in [44]

$$e[(1 - t_\varepsilon^\alpha)\bar{U}_j^n + t_\varepsilon^\alpha \hat{W}_j^\alpha] = \varepsilon \tag{2.49}$$

   – If $e(\hat{W}_j^\alpha) \geq \varepsilon$, let $t_\varepsilon^\alpha = 1$.
   Denote

$$\tilde{U}_{j+\frac{1}{2}}^- = \theta_2(\hat{U}_{j+\frac{1}{2}}^- - \bar{U}_j^n) + \bar{U}_j^n, \quad \tilde{U}_{j-\frac{1}{2}}^+ = \theta_2(\hat{U}_{j-\frac{1}{2}}^+ - \bar{U}_j^n) + \bar{U}_j^n.$$

5. The scheme (2.42) with the positivity-preserving limiter would be

$$\bar{U}_j^{n+1} = \bar{U}_j^n - \lambda(\hat{F}(\tilde{U}_{j+\frac{1}{2}}^-, \tilde{U}_{j+\frac{1}{2}}^+) - \hat{F}(\tilde{U}_{j-\frac{1}{2}}^-, \tilde{U}_{j-\frac{1}{2}}^+). \tag{2.50}$$

Remark 2 To prove that the limiter will not destroy the high order accuracy of density for smooth solutions, for a fifth order scheme, we need to show $\hat{\rho}_j(x) - \rho_j(x) = O(\Delta x^5)$ in (2.48). In the present compact scheme, although $\rho_{j+\frac{1}{2}}^-$ and $\rho_{j-\frac{1}{2}}^+$ are obtained globally, which are different from those in [42,44], the constructed polynomial $\rho_j(x)$ from (2.43) can be seen locally. Thus, the proof of preserving high order accuracy of density is similar to that in [42, 44]. Similar arguments hold for the internal energy. So the scheme (2.50) is conservative, high order accurate and positivity preserving.

2.5 Temporal discretization

Strong stability preserving (SSP) high order Runge-Kutta time discretization [16] will be used to improve the temporal accuracy for the scheme (2.50). The third-order SSP Runge-Kutta method is

$$U^{(1)} = U^n + \Delta t L(U^n),$$

$$U^{(2)} = \frac{3}{4}U^n + \frac{1}{4}U^{(1)} + \frac{1}{4}\Delta t L(U^{(1)}), \qquad (2.51)$$

$$U^{n+1} = \frac{1}{3}U^n + \frac{2}{3}U^{(2)} + \frac{2}{3}\Delta t L(U^{(2)}),$$

where $L(U)$ is the spatial operator. Similar to [44], for SSP high order time discretizations, the limiter will be used at each stage on each time step.

3 Numerical examples

In this section, we will investigate the numerical performance of the present positivity-preserving fifth-order finite volume compact-WENO (FVCW) scheme. The fifth-order WENO scheme [6] will be denoted as "WENO-Z" and the original fifth order WENO scheme of Jiang and Shu [19] is denoted as "WENO-JS". We will compare the FVCW scheme to WENO-JS and WENO-Z schemes. For all the numerical tests, the third-order SSP Runge-Kutta method (2.51) is used under the CFL condition (2.44) unless otherwise specified. The numerical solutions are computed with N grid nodes and up to time t.

Example 1 Advection of density perturbation. The initial conditions for density, velocity and pressure are specified, respectively, as

$$\rho(x,0) = 1 + 0.2sin(\pi x), \quad u(x,0) = 1, \quad p(x,0) = 1.$$

The exact solution of density is $\rho(x,t) = 1 + 0.2sin(\pi(x-t))$.

The computational domain is $[0,2]$ and the boundary condition is periodic. The L_1, L_2 and L_∞ errors and orders at $t = 2$ for the present finite volume compact-WENO scheme are shown in Table 3.1. Here the time step is taken to be $\Delta t = \frac{\omega_1}{\||u|+a\|}h^{5/3}$. We can clearly observe fifth-order accuracy for this problem.

In this example with smooth exact solutions, we also compare the computational cost between the FVCW scheme and the WENO-JS scheme. As we know, the FVCW scheme has high resolutions, however, a 3×3 block tri-diagonal system (2.21) needs to be solved at each grid node $x_{j+\frac{1}{2}}$ and at each stage of each time step. This might be computationally expensive. However, we will demonstrate by this example that the FVCW scheme would still be more efficient. Two kinds of reconstructions for systems are considered. One is based on a characteristic variable reconstruction, the other is directly reconstructing on the conservative variables. We take relatively coarser grids and choose the time step to satisfy $\lambda\||u|+a\| = 0.16$, so that the spatial error would always dominate. In Table 3.2, we show the computational cost between the FVCW scheme and the WENO-JS scheme for the conservative variable reconstruction case. For this case, without characteristic decomposition, only tri-diagonal (not block tri-diagonal) systems need to be solved along each component, less CPU cost would be needed. We can see at a comparable L_1 error level, the computational cost for the FVCW scheme is much less than the WENO-JS scheme especially when the error is small, which can also be seen from Fig.3.1 (left), where the comparison of the

Table 3.1 Numerical errors and orders for Example 1.

N	L_1 error	L_1 Order	L_∞ error	L_∞ Order	L_2 error	L_2 Order
10	7.802E-04		6.506E-04		5.874E-04	
20	1.493E-05	5.71	1.716E-05	5.24	1.263E-05	5.54
40	3.260E-07	5.52	2.942E-07	5.87	2.625E-07	5.59
80	9.107E-09	5.16	9.117E-09	5.01	7.162E-09	5.20
160	2.695E-10	5.08	2.903E-10	4.97	2.113E-10	5.08
320	8.169E-12	5.04	9.202E-12	4.98	6.413E-12	5.04

Table 3.2 Numerical errors and computational cost for WENO-JS and FVCW schemes for Example 1. Conservative variable reconstruction.

	FVCW					WENO-JS			
N	L_1 error	L_∞ error	L_2 error	CPU cost (s)	N	L_1 error	L_∞ error	L_2 error	CPU cost (s)
7	3.780E-03	2.796E-03	2.939E-03	1.56E-002	15	2.236E-03	1.899E-03	1.792E-03	3.13E-02
14	7.819E-05	8.125E-05	6.366E-05	3.12E-02	30	7.510E-05	7.187E-05	6.295E-05	0.11
28	2.065E-06	1.537E-06	1.579E-06	0.14	60	2.352E-06	2.353E-06	1.919E-06	0.47
56	5.879E-08	4.699E-08	4.511E-08	0.58	120	7.336E-08	7.082E-08	5.878E-08	1.88
112	1.945E-09	1.482E-09	1.506E-09	2.22	240	2.280E-09	2.022E-09	1.824E-09	7.55
224	8.882E-11	6.897E-11	6.926E-11	8.86	480	6.977E-11	5.909E-11	5.541E-11	29.95

Table 3.3 Numerical errors and computational cost for WENO-JS and FVCW schemes for Example 1. Characteristic variable reconstruction.

	FVCW					WENO-JS			
N	L_1 error	L_∞ error	L_2 error	CPU cost (s)	N	L_1 error	L_∞ error	L_2 error	CPU cost (s)
7	3.780E-03	2.796E-03	2.939E-03	3.13E-02	15	2.236E-03	1.899E-03	1.792E-03	4.69E-02
14	7.819E-05	8.125E-05	6.366E-05	0.11	30	7.509E-05	7.183E-05	6.293E-05	0.12
28	2.065E-06	1.537E-06	1.579E-06	0.47	60	2.351E-06	2.346E-06	1.917E-06	0.69
56	5.879E-08	4.699E-08	4.511E-08	1.86	120	7.318E-08	6.969E-08	5.859E-08	2.72
112	1.945E-09	1.482E-09	1.506E-09	7.34	240	2.259E-09	1.943E-09	1.802E-09	10.84
224	8.882E-11	6.898E-11	6.926E-11	29.22	480	6.800E-11	5.616E-11	5.377E-11	43.27

CPU cost versus the L_1 errors is displayed. Similarly in Table 3.3 and Fig. 3.1 (right) for the characteristic variable case, we can also observe less computational cost for the FVCW scheme when it has comparable error to the WENO-JS scheme. Similar discussions can be found in [13]. We note that the FVCW scheme with conservative variable reconstruction is more efficient than the characteristic variable reconstruction for smooth solutions. However for discontinuous solutions, the characteristic variable reconstruction would perform better to control spurious numerical oscillations. In this paper, for the following examples, we will mainly adopt the characteristic variable reconstruction.

Example 2 This example is the one-dimensional Lax shock tube problem [21] with the following Riemann initial conditions

$$(\rho, u, p) = \begin{cases} (0.445, 0.698, 3.528), & -5 \le x < 0, \\ (0.5, 0, 0.571), & 0 \le x < 5, \end{cases} \tag{3.1}$$

and the final time is $t = 1.4$.

(a) Conservative variable reconstruction
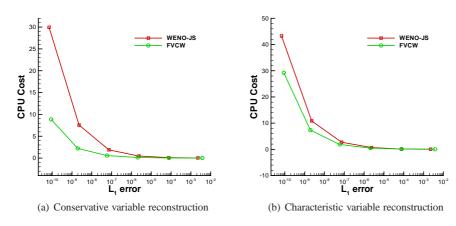
(b) Characteristic variable reconstruction

Fig. 3.1 Comparison of CPU cost versus L_1 errors for the WENO-JS and FVCW schemes. Left: conservative variable reconstruction in Table 3.2; Right: characteristic variable reconstruction in Table 3.3.

The exact solutions of a Lax problem contain a strong shock, a contact discontinuity and a rarefaction wave. We compute the solutions on the domain $[-5,5]$ with Neumann boundary conditions. The density and pressure on a grid of 200 points for the WENO-JS, WENO-Z and the present FVCW schemes are shown in Fig. 3.2. For this test problem, we observe the FVCW scheme is sharper than the WENO-JS and WENO-Z schemes, as it is less dissipative.

For this problem with discontinuous solutions, we also compare the WENO-JS scheme with the FVCW scheme at different grid nodes in Fig. 3.3. As we can see, the FVCW scheme with $N = 60$ and CPU cost $0.57s$ can match the result of the WENO-JS scheme with $N = 100$ and CPU cost $0.55s$, both are better than the WENO-JS scheme with $N = 60$. It shows the compact scheme has better resolutions than the non-compact scheme. At the same resolution, the compact scheme can take much coarser grids while with comparable computational cost as the non-compact scheme.

Example 3 This example is the one-dimensional Sod shock tube problem [35] with the following Riemann initial conditions

$$(\rho, u, p) = \begin{cases} (0.125, 0, 1), & -5 \leq x < 0, \\ (1, 0, 1), & 0 \leq x < 5, \end{cases} \tag{3.2}$$

and the final time is $t = 2.0$.

The exact solution contains a left-running rarefaction wave and a right-running contact discontinuity and a shock wave. The spatial domain $[-5,5]$ is discretized with 100 grid points and the results are shown in Fig.3.4. We compare our numerical results with those obtained by WENO-JS and WENO-Z schemes. The present scheme can capture the shock front and the contact discontinuity with correct locations and satisfactory sharpness. From Fig.3.4(b,c), we can observe that the numerical results obtained by the present FVCW scheme shows significant lower smearing across the discontinuities.
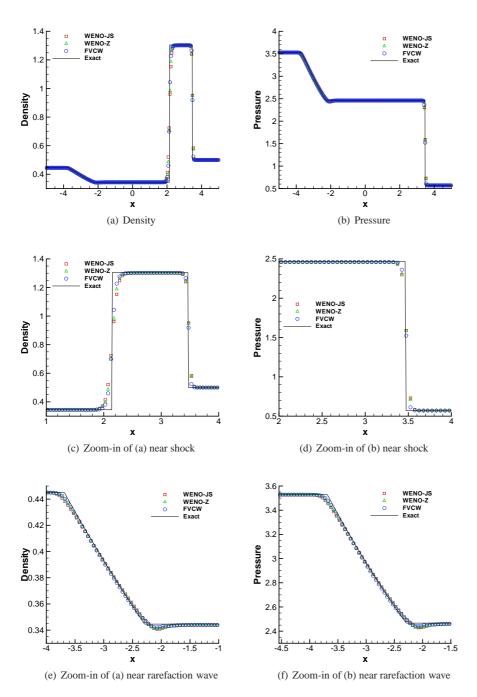
(a) Density

(b) Pressure

(c) Zoom-in of (a) near shock

(d) Zoom-in of (b) near shock

(e) Zoom-in of (a) near rarefaction wave

(f) Zoom-in of (b) near rarefaction wave

Fig. 3.2 The density (left) and pressure (right) profiles of the Lax problem (3.1) at $t = 1.4$.
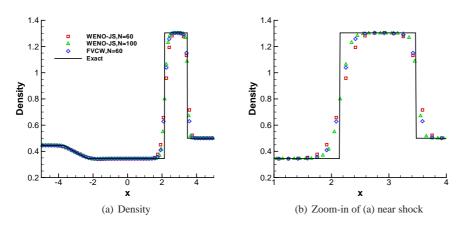
(a) Density (b) Zoom-in of (a) near shock

Fig. 3.3 The comparison of density for the Lax problem (3.1) with the WENO-JS scheme and the FVCW scheme at $t = 1.4$.

Example 4 In this example, the one dimensional Mach 3 shock-turbulence wave interaction problem [34] is tested with the following initial conditions

$$(\rho, u, p) = \begin{cases} (3.857143, 2.629369, 10.33333), & -5 \leq x < -4, \\ (1 + 0.2\sin 5x, 0, 1), & -4 \leq x < 5, \end{cases} \quad (3.3)$$

and the final time is $t = 1.8$. The solution of this problem consists of the interaction of a stationary shock and fine scale structures which are located behind a right-going main shock. As the density perturbation passes through the shock, it produces perturbations developing into the shock with smaller amplitude. Fig.3.5 shows the density on a grid of 200 points for the WENO-JS, WENO-Z and FVCW schemes. The "exact solution" is a reference solution computed by the WENO-JS scheme with 3200 grid points. It is observed that the present finite volume compact scheme captures the fine scale structures of the solution at the high-frequency waves behind the shock better than WENO-JS and WENO-Z, while also maintaining non-oscillatory behavior across the shock wave. The numerical solution is greatly improved with $N = 400$ and the numerical results are shown in Fig. 3.6.

Example 5 The one dimensional blastwave interaction problem of Woodward and Collela [38] has the following initial conditions

$$(\rho, u, p) = \begin{cases} (1, 0, 1000), & 0 \leq x < 0.1, \\ (1, 0, 0.01), & 0.1 \leq x < 0.9, \\ (1, 0, 100), & 0.9 \leq x \leq 1.0, \end{cases} \quad (3.4)$$

and reflective boundary conditions. The final time is $t = 0.038$. The initial pressure gradients generate two density shock waves which collide and interact at later time. The solution of this problem contains rarefactions, interaction of shock waves and the collision of strong shock waves. The "exact solution" of this test problem is a reference solution computed by the WENO-JS scheme with 3200 grid points. The density obtained with WENO-JS, WENO-Z and the present FVCW schemes at $t = 0.038$ with 200 cells are shown in Fig. 3.7. The zoomed regions of the density profile Fig. 3.7 (b) show that the present FVCW scheme gives better resolution than the other two schemes. The numerical solution is also greatly improved with $N = 400$ and the numerical results are shown in Fig. 3.8.
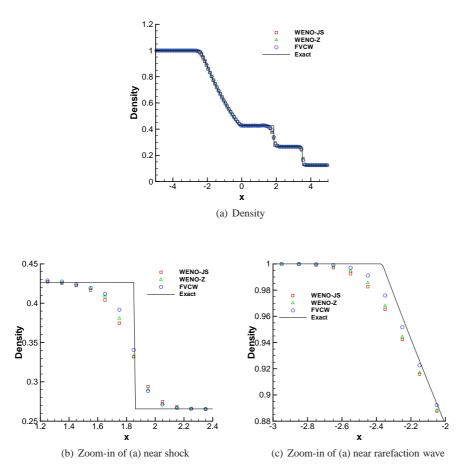
(a) Density

(b) Zoom-in of (a) near shock

(c) Zoom-in of (a) near rarefaction wave

Fig. 3.4 The density profiles of the Sod problem (3.2) at $t = 2.0$.

Example 6 In this test, we consider a one-dimensional low density and low internal energy Riemann problem with the following initial conditions

$$(\rho, u, p) = \begin{cases} (1, -2, 0.4), \ 0 \le x < 0.5, \\ (1, 2, 0.4), \quad 0.5 \le x < 1. \end{cases} \tag{3.5}$$

We take $h = 0.0025$ and the final time $t = 0.1$. The exact solution of this test consists of a trivial contact wave and two symmetric rarefaction waves. The results of the present positivity-preserving FVCW scheme with 400 cells compared with the exact solution are shown in Fig. 3.9. The minimum numerical values of the density and the internal energy are $1.835E - 02$ and $3.158E - 01$ respectively. For this problem, we can observe some oscillations in the central region, especially for the velocity and the internal energy. This might be due to the small density around that area and we have used a less dissipative HLLC flux. Slight oscillations on the density would cause very large oscillations on the velocity and the internal energy. The Lax-Friedrichs flux can be used to control the oscillations, we omit the results here to save space.
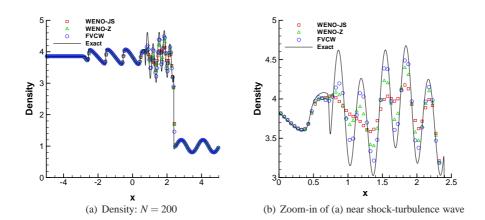
(a) Density: $N = 200$

(b) Zoom-in of (a) near shock-turbulence wave

Fig. 3.5 Shock-turbulence interaction (3.3) with $N = 200$ at $t = 1.8$.

(a) Density: $N = 400$

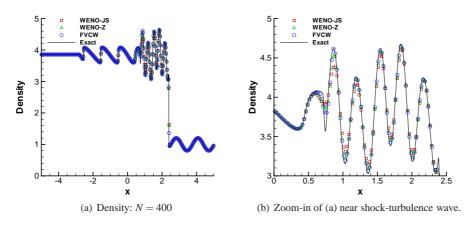(b) Zoom-in of (a) near shock-turbulence wave.

Fig. 3.6 Shock-turbulence interaction (3.3) with $N = 400$ at $t = 1.8$.

Example 7 In this test, a strong shock wave is generated by an extremely high pressure in the initial conditions

$$(\rho, u, p) = \begin{cases} (1, 0, 10^{10}), & 0 \leq x \leq 0.5, \\ (0.125, 0, 0.1), & 0.5 \leq x < 1, \end{cases} \tag{3.6}$$

with the final time $t = 2.5 \times 10^{-6}$. The results of the present positivity-preserving FVCW scheme with 200 cells compared with the exact solution are shown in Fig.3.10. The numerical solutions are very satisfactory in regard to numerical diffusion and spurious oscillations. The minimum numerical values of the density and the internal energy for this problem are $1.250E - 01$ and $2.000E + 00$ respectively. Both are positive.
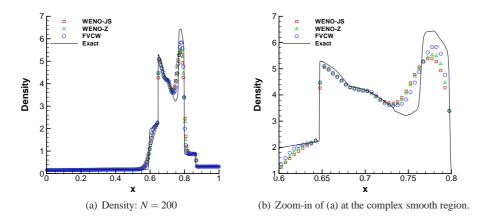
(a) Density: $N = 200$

(b) Zoom-in of (a) at the complex smooth region.

Fig. 3.7 Blastwave interaction problem (3.4) with $N = 200$ at $t = 0.038$.

(a) Density: $N = 400$

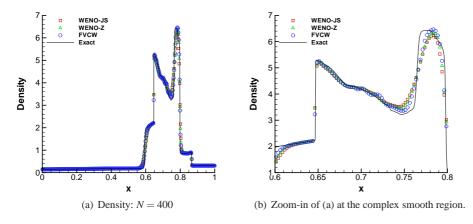(b) Zoom-in of (a) at the complex smooth region.

Fig. 3.8 Blastwave interaction problem (3.4) with $N = 400$ at $t = 0.038$.

Example 8 This one-dimensional test problem involves vacuum or near-vacuum solutions with the following initial conditions

$$(\rho, u, p) = \begin{cases} (7, -1, 0.2), & -1 \leq x < 0, \\ (7, -1, 0.2), & 0 \leq x \leq 1, \end{cases} \tag{3.7}$$

with $h = 0.005$ and the final time is $t = 0.6$. The computed pressure, density and velocity distributions are show in Fig. 3.11 (left). For this double rarefaction problem, the present FVCW scheme with the HLLC flux has comparable results as those in Zhang and Shu [46] (see their Fig. 5.1 (left)). The minimum numerical values of the density and the pressure are small positive values of $2.120E - 04$ and $2.201E - 04$ respectively. For this problem with vacuum or near-vacuum solutions, some oscillations can also be observed which might be due to the same reason as described in Example 6.
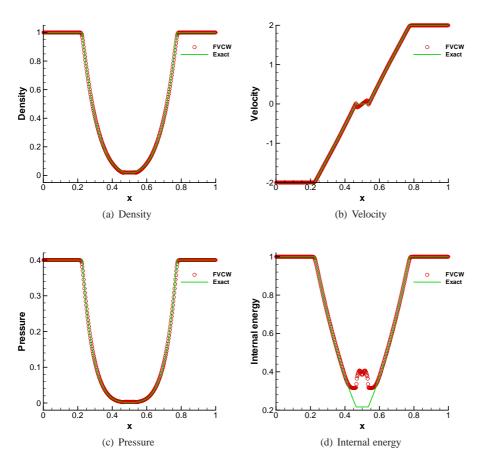
(a) Density

(b) Velocity

(c) Pressure

(d) Internal energy

Fig. 3.9 The results of the low density and low internal energy problem (3.5) with $N = 400$ at $t = 0.1$.

Example 9 This one-dimensional test problem is the planar Sedov blast-wave problem with the following initial conditions

$$(\rho, u, p) = \begin{cases} (1, 0, 4 \times 10^{-13}), & 0 < x \le 2 - 0.5h, \, 2 + 0.5h < x < 4, \\ (1, 0, 2.56 \times 10^8), & 2 - 0.5h < x \le 2 + 0.5h, \end{cases} \tag{3.8}$$

with $h = 0.005$ and the final time is $t = 0.001$. The numerical results of the present positivity-preserving fifth order finite volume compact-WENO scheme are shown in Fig.3.11 (right). By comparing with Zhang and Shu [46] (see their Fig. 5.1 (right)) for the planar Sedov blast-wave problem, we can observe that a slightly sharper blast wave is obtained by using the present FVCW scheme. The minimum numerical values of the density and the internal energy are also small positive values of $4.731E - 03$ and $1.000E - 12$ respectively.

Example 10 LeBlanc shock tube problem. In this extreme shock tube problem, the computational domain is [0,9] filled with a perfect gas with $\gamma = 5/3$. The initial conditions are with high ratio of jumps for the internal energy and density. The jump for the internal energy is
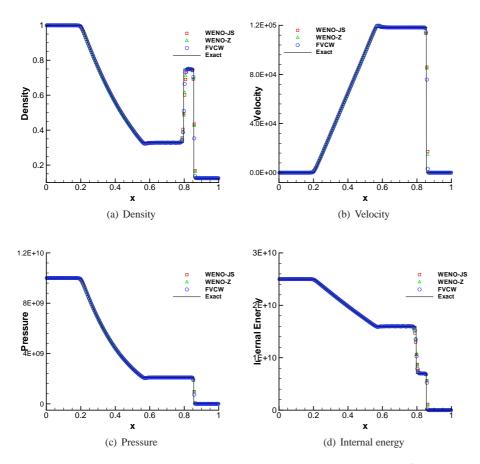
(a) Density

(b) Velocity

(c) Pressure

(d) Internal energy

Fig. 3.10 The results of the strong shock wave problem (3.6) with $N = 200$ at $t = 2.5 \times 10^{-6}$.

10^6 and the jump for the density is 10^3. The initial conditions are given by

$$(\rho, u, e) = \begin{cases} (1, 0, 0.1), & 0 \le x < 3, \\ (0.001, 0, 10^{-7}), & 3 < x \le 9. \end{cases} \qquad (3.9)$$

The solution consists of a strong rarefaction wave moving to the left, a contact discontinuity and a shock moving to the right. The difficulty for numerical simulations of this problem can be found in [24, 7, 27]. Numerical results obtained with the present FVCW schemes at $t = 6.0$ with 400 and 1000 cells are shown in Fig.3.12. By comparing with the exact solutions, we can observe that the present FVCW scheme preserves positive density and internal energy, and the minimum numerical values for density and pressure are $1.000E - 03$ and $1.000E - 07$ respectively. An overshoot is produced, especially for the internal energy, however similar results are obtained in [24, 7, 27]. Fig.3.12 shows that the numerical solution is greatly improved as the mesh is refined.
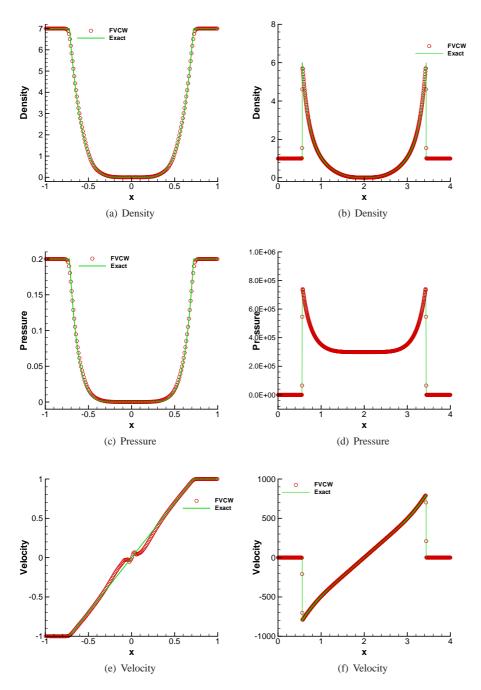
(a) Density

(b) Density

(c) Pressure

(d) Pressure

(e) Velocity

(f) Velocity

Fig. 3.11 One-dimensional problems involving vacuum or near vacuum, $h = 0.005$: (left) double rarefaction problem (3.7) at $t = 0.6$; (right) planar Sedov blast-wave problem (3.8) at $t = 0.001$.
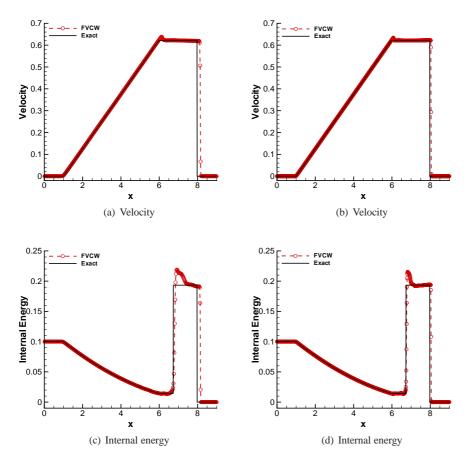
(a) Velocity

(b) Velocity

(c) Internal energy

(d) Internal energy

Fig. 3.12 The results of the Leblanc problem (3.9) at $t = 6.0$. $N = 400$ (left), $N = 1000$ (right).

4 Conclusions

In this paper, we have developed a positivity-preserving fifth-order finite volume compact-WENO scheme for compressible Euler equations in one dimension. Compared to finite difference compact-reconstruction WENO schemes proposed by Ghosh et. al. [13], the positivity-preserving limiter is used to preserve positive density and internal energy under a finite volume framework. An approximate HLLC Riemann solver is used due to its less dissipation and robustness. The present scheme increases spectral properties of the classical WENO schemes. Compared to classical fifth order finite volume compact schemes, the present scheme keeps the essentially non-oscillatory properties for capturing discontinuities. Numerical results have shown that the present scheme is positivity preserving, high order accurate, and can produce superior resolutions compared to the classical WENO schemes. Extension the FVCW scheme to multi-dimensional problems contributes our future work.

References

1. N. ADAMS AND K. SHARIFF, *A high-resolution hybrid compact-ENO scheme for shock-turbulence interaction problems*, Journal of Computational Physics, 127 (1996), pp. 27–51.
2. D. S. BALSARA, *Self-adjusting, positivity preserving high order schemes for hydrodynamics and magnetohydrodynamics*, Journal of Computational Physics, 231 (2012), pp. 7504–7517.
3. D. S. BALSARA AND C.-W. SHU, *Monotonicity preserving weighted essentially non-oscillatory schemes with increasingly high order of accuracy*, Journal of Computational Physics, 160 (2000), pp. 405–452.
4. P. BATTEN, N. CLARKE, C. LAMBERT, AND D. CAUSON, *On the choice of wavespeeds for the HLLC Riemann solver*, SIAM Journal on Scientific Computing, 18 (1997), pp. 1553–1570.
5. R. BORGES, M. CARMONA, B. COSTA, AND W. DON, *An improved weighted essentially non-oscillatory scheme for hyperbolic conservation laws*, Journal of Computational Physics, 227 (2008), pp. 3191–3211.
6. M. CASTRO, B. COSTA, AND W. DON, *High order weighted essentially non-oscillatory WENO-Z schemes for hyperbolic conservation laws*, Journal of Computational Physics, 230 (2011), pp. 1766–1792.
7. J. CHENG AND C.-W. SHU, *Positivity-preserving Lagrangian scheme for multi-material compressible flow*, Journal of Computational Physics, 257 (2014), pp. 143–168.
8. B. COCKBURN AND C.-W. SHU, *Nonlinearly stable compact schemes for shock calculations*, SIAM Journal on Numerical Analysis, 31 (1994), pp. 607–627.
9. X. DENG AND H. MAEKAWA, *Compact high-order accurate nonlinear schemes*, Journal of Computational Physics, 130 (1997), pp. 77–91.
10. X. DENG AND H. ZHANG, *Developing high-order weighted compact nonlinear schemes*, Journal of Computational Physics, 165 (2000), pp. 22–44.
11. B. EINFELDT, C.-D. MUNZ, P. L. ROE, AND B. SJÖGREEN, *On godunov-type methods near low densities*, Journal of computational physics, 92 (1991), pp. 273–295.
12. J. ESTIVALEZES AND P. VILLEDIEU, *High-order positivity-preserving kinetic schemes for the compressible euler equations*, SIAM Journal on Numerical Analysis, 33 (1996), pp. 2050–2067.
13. D. GHOSH AND J. BAEDER, *Compact Reconstruction Schemes with Weighted ENO Limiting for Hyperbolic Conservation Laws*, SIAM Journal on Scientific Computing, 34 (2012), pp. 1678–1706.
14. S. K. GODUNOV, *A differerence method for the numerical calculation of discontinuous solutions of hydrodynamic equations*, Mathematicheskii Sbornik, 89 (1959), pp. 271–306.
15. Y. GONG AND Y. X. LONG, *LU method for solving block tridiagonal matrix equations and its applications*, Journal of Dalian University of Technology, 37 (1997), pp. 406–409.
16. S. GOTTLIEB, D. KETCHESON, AND C.-W. SHU, *High order strong stability preserving time discretizations*, Journal of Scientific Computing, 38 (2009), pp. 251–289.
17. J. GRESSIER, P. VILLEDIEU, AND J.-M. MOSCHETTA, *Positivity of flux vector splitting schemes*, Journal of Computational Physics, 155 (1999), pp. 199–220.
18. X. Y. HU, N. A. ADAMS, AND C.-W. SHU, *Positivity-preserving method for high-order conservative schemes solving compressible euler equations*, Journal of Computational Physics, 242 (2013), pp. 169–180.
19. G.-S. JIANG AND C.-W. SHU, *Efficient implementation of weighted ENO schemes*, Journal of Computational Physics, 126 (1996), pp. 202–228.
20. L. JIANG, H. SHAN, AND C. LIU, *Weighted compact scheme for shock capturing*, International Journal of Computational Fluid Dynamics, 15 (2001), pp. 147–155.
21. P. D. LAX, *Weak solutions of nonlinear hyperbolic equations and their numerical computation*, Communications on Pure and Applied Mathematics, 7 (1954), pp. 159–193.
22. S. LELE, *Compact finite difference schemes with spectral-like resolution*, Journal of Computational Physics, 103 (1992), pp. 16–42.
23. R. J. LEVEQUE, *Finite volume methods for hyperbolic problems*, vol. 31, Cambridge university press, 2002.
24. W. LIU, J. CHENG, AND C.-W. SHU, *High order conservative Lagrangian schemes with Lax–Wendroff type time discretization for the compressible Euler equations*, Journal of Computational Physics, 228 (2009), pp. 8872–8891.

25. X. LIU, S. OSHER, AND T. CHAN, *Weighted essentially non-oscillatory schemes*, Journal of Computational Physics, 115 (1994), pp. 200–212.
26. X. LIU, S. ZHANG, H. ZHANG, AND C.-W. SHU, *A new class of central compact schemes with spectral-like resolution i: Linear schemes*, Journal of Computational Physics, 248 (2013), pp. 235–256.
27. R. LOUBÈRE AND M. J. SHASHKOV, *A subcell remapping method on staggered polygonal grids for arbitrary-Lagrangian–Eulerian methods*, Journal of Computational Physics, 209 (2005), pp. 105–138.
28. B. PERTHAME, *Boltzmann type schemes for gas dynamics and the entropy property*, SIAM Journal on Numerical Analysis, 27 (1990), pp. 1405–1421.
29. B. PERTHAME AND C.-W. SHU, *On positivity preserving finite volume schemes for Euler equations*, Numerische Mathematik, 73 (1996), pp. 119–130.
30. S. PIROZZOLI, *Conservative hybrid compact-WENO schemes for shock-turbulence interaction*, Journal of Computational Physics, 178 (2002), pp. 81–117.
31. Y. REN, M. LIU, AND H. ZHANG, *A characteristic-wise hybrid compact-WENO scheme for solving hyperbolic conservation laws*, Journal of Computational Physics, 192 (2003), pp. 365–386.
32. Y. SHEN, G. YANG, AND Z. GAO, *High-resolution finite compact difference schemes for hyperbolic conservation laws*, Journal of Computational Physics, 216 (2006), pp. 114–137.
33. C. SHU, *Essentially non-oscillatory and weighted essentially non-oscillatory schemes for hyperbolic conservation laws*, Advanced numerical approximation of nonlinear hyperbolic equations, (1998), pp. 325–432.
34. C.-W. SHU AND S. OSHER, *Efficient implementation of essentially non-oscillatory shock-capturing schemes, ii*, Journal of Computational Physics, 83 (1989), pp. 32–78.
35. G. A. SOD, *A survey of several finite difference methods for systems of nonlinear hyperbolic conservation laws*, Journal of Computational Physics, 27 (1978), pp. 1–31.
36. T. TAO AND K. XU, *Gas-kinetic schemes for the compressible Euler equations: positivity-preserving analysis*, Zeitschrift für angewandte Mathematik und Physik ZAMP, 50 (1999), pp. 258–281.
37. E. F. TORO, *Riemann solvers and numerical methods for fluid dynamics: a practical introduction*, Springer, 2009.
38. P. WOODWARD AND P. COLELLA, *The numerical simulation of two-dimensional fluid flow with strong shocks*, Journal of Computational Physics, 54 (1984), pp. 115–173.
39. T. XIONG, J.-M. QIU, AND Z. XU, *Parametrized Positivity Preserving Flux Limiters for the High Order Finite Difference WENO Scheme Solving Compressible Euler Equations*, submitted, (2013).
40. S. ZHANG, X. DENG, M. MAO, AND C. SHU, *Improvement of convergence to steady state solutions of Euler equations with weighted compact nonlinear schemes*, Acta Mathematicae Applicatae Sinica, 29 (2013), pp. 449–464.
41. S. ZHANG, S. JIANG, AND C. SHU, *Development of nonlinear weighted compact schemes with increasingly higher order accuracy*, Journal of Computational Physics, 227 (2008), pp. 7294–7321.
42. X. ZHANG AND C. SHU, *Maximum-principle-satisfying and positivity-preserving high-order schemes for conservation laws: survey and new developments*, Proceedings of the Royal Society A: Mathematical, Physical and Engineering Science, 467 (2011), pp. 2752–2776.
43. X. ZHANG AND C.-W. SHU, *On maximum-principle-satisfying high order schemes for scalar conservation laws*, Journal of Computational Physics, 229 (2010), pp. 3091–3120.
44. ——, *On positivity-preserving high order discontinuous galerkin schemes for compressible euler equations on rectangular meshes*, Journal of Computational Physics, 229 (2010), pp. 8918–8934.
45. ——, *Positivity-preserving high order discontinuous Galerkin schemes for compressible Euler equations with source terms*, Journal of Computational Physics, 230 (2011), pp. 1238–1248.
46. ——, *Positivity-preserving high order finite difference WENO schemes for compressible Euler equations*, Journal of Computational Physics, 231 (2012), pp. 2245–2258.
47. X. ZHANG, Y. XIA, AND C.-W. SHU, *Maximum-principle-satisfying and positivity-preserving high order discontinuous Galerkin schemes for conservation laws on triangular meshes*, Journal of Scientific Computing, 50 (2012), pp. 29–62.